Mühendislik Bilimleri ve Tasarım Dergisi
14(1), 150-169, 2026
e-ISSN: 1308-6693

Journal of Engineering Sciences and Design
DOI: 10.21923/jesd.1856770

Araştırma Makalesi Research Article

HIGH-SENSITIVITY DETECTION OF PARTIAL DISCHARGE-INDUCING VOIDS IN MEDIUM VOLTAGE XLPE CABLES USING A NOVEL SRR-BASED MICROWAVE SENSOR

Mustafa YILDIRIM[1], Mahmut Ahmet GÖZEL[1*], Celal Fadıl KUMRU[1]

[1] Department of Electrical and Electronics Engineering, Faculty of Engineering and Natural Sciences, Suleyman Demirel University, Isparta, Türkiye

Keywords

XLPE, Medium Voltage, Electricity, Partial Discharge, Microwave Sensor.

Abstract

Air voids within the insulation layer of high-voltage power cables constitute a significant threat to system reliability by triggering partial discharge (PD) events, which can eventually lead to catastrophic insulation breakdown. In this study, a Split Ring Resonator (SRR) sensor based on the microwave resonance technique was designed and experimentally validated for the non-destructive detection of air voids in XLPE cable insulation. Distinct from existing literature, which predominantly utilizes antenna-based structures to capture PD signals via reflection coefficients (S_{11}), this work employs a transmission line-based sensor to detect local dielectric changes directly through transmission parameter (S_{21}) monitoring. The developed sensor induced significant resonance frequency shifts based on the principle that air voids reduce the effective dielectric constant. Experimental analyses demonstrated that the sensor possesses sufficient penetration depth to analyze the internal structure despite the shielding effects of the semiconductor layer and the outer protective sheath. In full-scale cable tests, the reference resonance frequency of 4.42 GHz shifted to 4.60 GHz for the dominant volumetric void, 4.56 GHz for the narrow void, and 4.54 GHz for the shallow void. With frequency differences reaching up to 460 MHz relative to the reference state, the sensor enabled both defect detection and characterization.

ORTA GERİLİM XLPE KABLOLARINDA KISMİ DEŞARJA NEDEN OLAN BOŞLUKLARIN ÖZGÜN BİR SRR TABANLI MİKRODALGA SENSÖR İLE YÜKSEK HASSASİYETLİ TESPİTİ

Anahtar Kelimeler Öz

Orta Gerilim, Elektrik, Kısmi Desarj, XLPE, Mikrodalga Sensör.

Yüksek gerilim güç kablolarının yalıtım katmanı içindeki hava boşlukları, yalıtım delinmesine yol açabilen kısmi deşarj (PD) olaylarını tetikleyerek sistem güvenilirliği için bir tehdit oluşturur. Bu çalışmada, XLPE kablo yalıtımında hava boşluklarının tahribatsız tespiti için mikrodalga rezonans tekniğine dayalı Ayrık Halka Rezonatör sensörü tasarlanmış ve deneysel olarak doğrulanmıştır. Genellikle anten tabanlı yapılar kullanarak S_{11} parametresi aracılığıyla PD sinyallerini tespit etmeye odaklanan literatürdeki çalışmaların aksine, bu çalışma iletim hattı tabanlı bir sensör kullanarak dielektrik değişimleri doğrudan tespit etmeyi amaçlamaktadır. Geliştirilen sensör, hava boşluklarının ortamın etkin dielektrik sabitini azaltması prensibine dayanarak rezonans frekansında değişikliklere neden olmuştur. Deneysel analizler, sensörün yarı iletken katmanın ve dış koruyucu kılıfın kalkanlama etkilerine rağmen iç yapıyı analiz etmek için yeterli nüfuz derinliğine sahip olduğunu göstermiştir. Saha koşullarını simüle eden tam kablo yapısında, rezonans frekansı kusursuz referans durumunda 4.42 GHz olarak ölçülmüştür. Bu frekans değeri, hacimsel boşluğun en baskın olduğu senaryoda 4.60 GHz'e, dar/derin boşluk için 4.56 GHz'e ve sığ boşluk için 4.54 GHz'e değişmiştir. Referans durumuna göre 460 MHz'e varan frekans farkları, sadece kusurun tespit edilmesini değil, aynı zamanda büyüklüğünün ve özelliklerinin de analiz edilmesini sağlamıştır.

Alıntı / Cite

YILDIRIM, M., GÖZEL, M. A., KUMRU, C. F., (2026). High-Sensitivity Detection of Partial Discharge-Inducing Voids in Medium Voltage XLPE Cables Using a Novel SRR-Based Microwave Sensor, Journal of Engineering Sciences and Design, 14(1), 150-169.

Yazar Kimliği / Author ID (ORCID Number)

M. Yıldırım, 0000-0002-5675-1714
M. A. Gözel, 0000-0002-0360-7188
C. F. Kumru, 0000-0003-4248-6355

Makale Süreci / Article Process

Başvuru Tarihi / Submission Date	05.01.2026
Revizyon Tarihi / Revision Date	09.01.2026
Kabul Tarihi / Accepted Date	23.01.2026
Yayım Tarihi / Published Date	20.03.2026

[*]İlgili Yazar / Corresponding author: mahmutgozel@sdu.edu.tr, +90 0246 211 1514

HIGH-SENSITIVITY DETECTION OF PARTIAL DISCHARGE-INDUCING VOIDS IN MEDIUM VOLTAGE XLPE CABLES USING A NOVEL SRR-BASED MICROWAVE SENSOR

Mustafa YILDIRIM[1], Mahmut Ahmet GÖZEL[†1], Celal Fadıl KUMRU[1]
Department of Electrical and Electronics Engineering, Faculty of Engineering and Natural Sciences, Suleyman Demirel University, Isparta, Türkiye

Highlights

- An SRR-based microwave sensor is proposed for air void detection in XLPE cable insulation.
- The partial discharge region is directly identified using the S21 transmission parameter.
- The method enables early, non-invasive detection of insulation defects in MV power cables.

Graphical Abstract

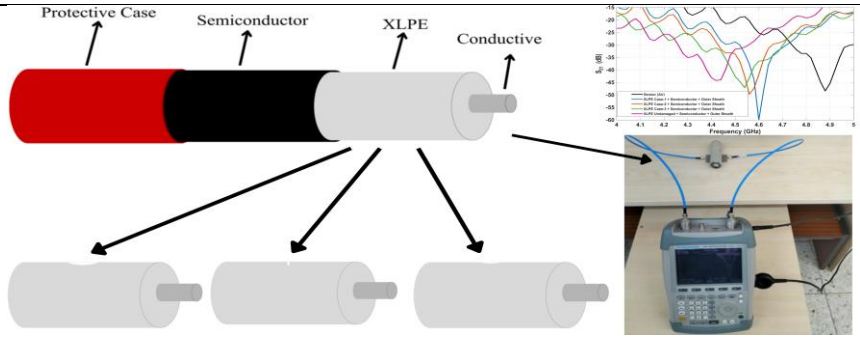

Figure. Artificial defect geometries modeled in XLPE cable insulation, measurement setup, and S_{21} results for different damage scenarios

Purpose and Scope

The aim of this study is to design, optimize, and validate a microwave sensor based on a split ring resonator (SRR) for detecting air voids that may occur within the insulation of medium-voltage XLPE cables in order to prevent partial discharge (PD) activity. The study focuses on the early detection of insulation defects by employing high-frequency electromagnetic sensing principles and aims to provide a reliable and non-invasive monitoring approach for medium-voltage power cables.

Design/methodology/approach

The research objectives were achieved by designing and optimizing the geometry of an SRR-based microwave sensor through electromagnetic simulations. The sensor performance was evaluated based on resonance frequency shifts and S-parameters, while the effects of air voids of different sizes and locations on the dielectric properties were investigated through theoretical and numerical analyses.

Findings

The results clearly demonstrate that the proposed SRR-based microwave sensor exhibits high sensitivity to air voids within the insulation of XLPE cables. While the resonance frequency of the sensor in free space (air environment) was measured as 4.88 GHz, this value decreased to 4.42 GHz in the reference case of a perfect, defect-free cable, corresponding to a total frequency shift of 460 MHz. For the different damage scenarios represented by Case 1, Case 2, and Case 3, the resonance frequencies were obtained as 4.60 GHz, 4.56 GHz, and 4.54 GHz, with corresponding frequency shifts of 280 MHz, 320 MHz, and 340 MHz, respectively.

Research limitations/implications

This study was conducted under controlled laboratory conditions and based on idealized modeling assumptions. In real field environments, environmental factors such as temperature, humidity, mechanical stresses, and manufacturing tolerances may affect the sensor performance.

Practical implications

The proposed sensor enables online and non-invasive monitoring of insulation health in medium-voltage power cables. This approach can contribute to reducing unplanned power outages, lowering maintenance costs, and improving the operational reliability of power systems.

Originality

This study presents an SRR-based microwave sensor within an original design framework for detecting air voids in medium-voltage XLPE cable insulation.

[†] Corresponding author: mahmutgozel@sdu.edu.tr, +90 0246 211 1514

1. Introduction

Medium voltage (MV) cables are considered one of the most critical components of distribution networks in terms of providing transmission between energy production and consumption points. Cross-linked polyethylene (XLPE) cables, which are widely preferred in underground energy transmission, are seen to consist of intertwined coaxial layers, including the current carrier conductor in the center, the XLPE layer that provides the main insulation, the semiconductor layers that regulate the electric field distribution, and the outer sheath that acts as mechanical protection (Densley, 2002; Vogelsang et al., 2009). Within this multi-layered structure, XLPE insulator constitutes the most critical component of the system due to its high dielectric strength. However, these cables operated in underground networks are also frequently exposed to external mechanical influences such as excavation work or ground movements. Depending on operating difficulties or environmental changes in underground conditions, large or small air gaps may occur in the insulating material. Application errors in the repair processes of damaged cables and neglect of visible or invisible defects in the XLPE insulator material are another critical risk factor. In particular, despite repairing the outer protective sheath and semiconductor layers, ignoring microcracks or cuts on the XLPE insulator layer disrupts the insulator integrity, resulting in a local reduction in dielectric strength (Arikan et al., 2023; Chimunda & Nyamupangedengu, 2019; Forssen & Edin, 2008; Zhang et al., 2018). The air gaps in question have a lower dielectric coefficient compared to XLPE material, leading to the concentration of local electric field strength at these defective points. This field condensation, which has reached a critical level, causes the gas in the cavity to ionize, paving the way for the initiation of local electrical discharges, which are defined as "Partial Discharge" (PD) in the literature. These electrical discharges disrupt the chemical structure of the insulating material over time, leading to the formation of electrical treeing and eventual perforation of the cable (Illias et al., 2011; Liu et al., 2017) Traditional electrical measurement methods based on the IEC 60270 standard, acoustic emission sensors and High Frequency Current Transformers (HFCT) are widely used in the literature for the detection of defects in cable insulators (Yaacob et al., 2014) . In an important study in the literature focusing on the multidimensional analysis of cable insulation performance, the effects of different electrical stresses such as overvoltage and impulse voltage on aging mechanisms were examined (Kumru et al., 2023). Analyses on 12/20.8 kV XLPE cables showed that the DDF method needed historical data due to its oscillation; on the other hand, the PD method followed a more stable course, especially the effects of impulse voltage. revealed that it exhibited superior performance in the evaluation. In the light of these findings, the inadequacy of a single method was emphasized and a hybrid procedure was proposed to increase diagnostic reliability (Arikan et al., 2023) However, the limitations of traditional methods in noise sensitivity and pinpoint detection pose challenges in field applications. For this reason, there is a growing interest in microwave sensor technologies that can detect even the smallest changes in the dielectric properties of the insulator with high sensitivity. (Chai et al., 2019; Gocen & Palandoken, 2023; Shibuya et al., 2010).

In the literature, microwave sensors appear to be widely used in studies such as liquid content analysis (Palandoken & Gocen, 2025a; Palandoken et al., 2023; Yıldırım & Gözel, 2023) and characterization of solid materials (Kiani et al., 2018). In applications requiring high accuracy and precise measurement, such as material characterization, various methods have been developed to enhance the detection capability of sensors (Palandoken & Gocen, 2025b). Among these methods; Constituent Discrete Ring Resonator (SRR) [(Gocen & Palandoken, 2024), Complementary Discrete Ring Resonator (CSRR) [(Han, Liu, Zhang, et al., 2024) and metamaterial(Hossen et al., 2025) stand out. Thanks to the strong electric field they provide, these structures allow even the smallest changes in the dielectric constant of the tested material to be detected with high precision. In the study of a directional coupler integrated multiple CSRR-based four-port sensor presented in the literature, characterization of solid dielectrics in the L and S bands was performed. In this structure, where transmission (S_{21}), coupling (S_{31}) and isolation (S_{41}) parameters and sample thickness are analyzed simultaneously; High sensitivity of 7.5% and frequency resolution of 210.8 MHz have been achieved. In addition, the maximum error rate has been reduced to as low as 0.48% (Genç et al., 2025). A new sensor architecture with an elliptical structure based on CEE-LC resonator and branched line coupler has been developed for milk fat content and adulteration analysis in food safety applications. A precision of over 1% has been achieved in measurements made with a VCO integrated portable system. In water adulteration analyses, the resonance frequency showed a linear change from 2.40 GHz to 2.105 GHz; and the increase in oil ratio increased the DC output voltage in the range of 1.23–1.56 V. The study results reveal that multi-port sensor structures enable precise dielectric analysis in a field setting without the need for laboratory setups (Yıldırım & Gözel, 2025). In a theoretical and experimental study in the literature examining the performance of patch antennas as PD sensors, electromagnetic waves originating PD were analyzed using the antenna and transmission line model. As a result of EMTP simulations performed with the assumption of Gaussian current distribution, it was determined that the antenna sensitivity is largely dependent on the development rate of the PD current and that the detection sensitivity increases as the discharge time is shortened (Shibuya et al., 2010). The application area of microwave sensors is not limited to the characterization of liquid or solid materials. These structures can also be used effectively to detect local deformations such as air

gaps or cracks that may occur in the material through the change in the dielectric constant of the environment (Zarifi et al., 2017).

In another study in the literature focusing on the detection of voids in concrete-based composite structures, a new microwave dual waveguide sensor operating in the X-band frequency range was proposed. Within the scope of the study, the sensor structure consisting of two waveguide sections embedded in the metal plate; It was both experimentally tested on concrete-metal and concrete-dielectric layer-metal samples and modeled in the CST Microwave Studio environment. Through the developed algorithms and simulations, the complex dielectric permeability of the concrete in the measurement area was determined and the reflection and conduction coefficients were analyzed with reference to the gap-free state. The findings show that the reflection coefficient measurements can successfully detect small air gaps between 0 mm and 2 mm in both composite structures. On the other hand, it has been reported that conduction measurements give more reliable results in the detection of gaps at the level of <0.5 mm for concrete-dielectric layer-metal structures and >0.5 mm for concrete-metal structures. The high agreement between the measurement and simulation results reveals that the proposed system is an effective method for the precise evaluation of even micrometer-level voids in composite structures such as concrete-filled steel pipes (Islam & Kharkovsky, 2016). For partial discharge (PD) monitoring in high and medium voltage equipment, an ultra-wideband (UWB) microstrip antenna has been designed that suppresses low-frequency ambient noises (GSM, etc.) and operates in the 1.2–4.5 GHz band. The design, performed on an FR-4 substrate, demonstrated simulation and measurement alignment with return loss performance below -10 dB. In experimental analyses, a signal amplitude of 248 mV was obtained against background noise at the level of 6 mV, confirming the high sensitivity. In comparative tests with commercial HFCT sensors, the antenna was reported to provide PDIV values consistent with the reference sensor up to a distance of 70 cm and was an effective sensor candidate for non-invasive PD monitoring applications (Uwiringiyimana et al., 2022). Insulation aging and manufacturing defects or Partial Discharge (PD) activities originating from cable repair are a critical risk factor for the sustainability of high voltage systems. Although RF-based detection methods offering EMI immunity are widely accepted in the literature, microwave sensor studies in this field have been predominantly limited to antenna-based topologies (Kaziz et al., 2023). Antenna structures can confirm the presence of discharge by capturing the emitted electromagnetic waves; However, due to the nature of the radiation patterns, the position of microscopic gaps in the cable insulator cannot provide the high spatial resolution required to detect.

When the studies in literature are examined, it is seen that microwave sensors offer effective solutions for material characterization and content analysis. However, the number of microwave studies to detect microscopic air gaps within the multi-layer structure of XLPE power cables with cylindrical geometry with high precision without compromising the cable integrity is limited. In this study, a new microwave sensor design with a transmission line-based and multi-layer SRR structure is proposed in order to prevent partial discharge (PD) failures in medium voltage cables. The multi-layered SRR structure of the designed sensor concentrates the electric field, allowing even the smallest dielectric changes on the XLPE insulator to be detected. Within the scope of the study, it was aimed to determine the air gaps in the insulator through the change in the resonance frequency of the sensor with separate measurements on XLPE insulator, semiconductor layer and protective sheaths. Thus, it is aimed at identifying defective areas before the cable fails and to minimize possible PD risks.

2. Partial Discharge Mechanisms and Air Void Effects

Partial discharge (PD) is a localized dielectric puncture event that occurs only in a limited region in an electrical insulation system with solid, liquid, or gas insulation media, without bridging the gap between two conductors to cover the entire insulation. This phenomenon occurs because of electric field densities that occur within the insulation structure and locally exceed the dielectric strength limit. Since the 1990s, numerous experimental and theoretical studies have been carried out on the understanding, perception and characterization of partial discharge mechanisms (R Bartnikas, 2002; Ray Bartnikas, 2002; Kreuger et al., 2002). The stochastic nature of the PD phenomenon is based on the random distribution of initiator electrons and the fact that the charges left by previous discharges on the dielectric surface (memory effect) affect subsequent events (Ray Bartnikas, 2002; Niemeyer, 2002). Although these uncertainties complicate the diagnostic process, discharge mechanisms are mainly classified under four main headings: internal discharge, treeing discharge, surface discharge, and corona discharge, and this classification is shown in Figure 1.

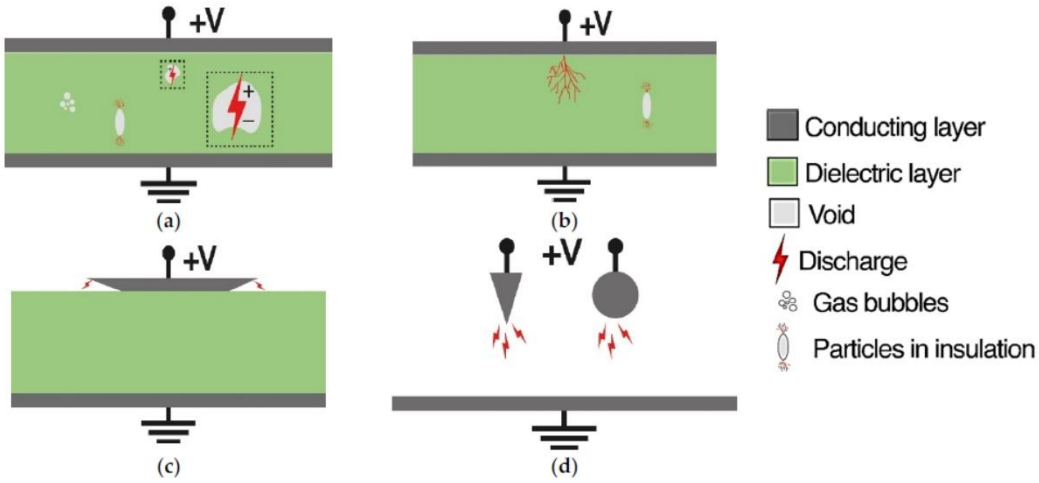

Figure 1. Different types of partial discharge: (a) Internal discharge, (b) Treeing, (c) Surface discharge, and (d) Corona discharge (Kaziz et al., 2023).

Partial discharges (PD) are considered in four main classes: internal, treeing, surface and corona discharges, as shown in Figure 1. Internal partial discharges are one of the most common and dangerous types of PD and occur when micro-scale air gaps trapped in the dielectric structure during the manufacturing process create an unbalanced electric field distribution with the surrounding dielectric under high voltage, and usually the insulation is removed early without any symptoms before failure. It causes deterioration. Reforestation discharges, on the other hand, develop in the form of electrical channels that spread from starting points such as mechanical defects, gas cavities or impurities and exhibit a branched structure; It progresses under prolonged and repetitive electrical stress, severely reducing the dielectric strength of the insulation and ultimately resulting in a complete puncture. Surface discharges occur on solid insulating surfaces due to the tangential components of the electric field and become especially evident in humid and polluted environments, while corona discharges occur as a result of conductors with sharp geometric irregularities being exposed to high areal densities in the air environment, often manifest themselves with a visible glow and are generally considered less harmful compared to other types of PD (Dissado, 2002; Niemeyer, 2002).

In the case of air or gas-filled cavities within solid insulating materials, the electric field distribution becomes inhomogeneous due to the relative dielectric constant difference between the material and the vacancy. The relative dielectric constant of the cavity ($\varepsilon_{rc} \approx 1$) is usually considerably smaller than the relative dielectric constant ($\varepsilon_{ra} > 1$) of the surrounding solid insulator. This leads to the concentration of the electric field within the cavity under the applied voltage, causing the in-cavity field strength to increase significantly compared to the surrounding material. As a result, a partial discharge occurs when the electric field in the cavity exceeds the puncture strength of the gas. This phenomenon can be expressed quantitatively by modeling the rigid insulator-cavity system as series-connected capacities.

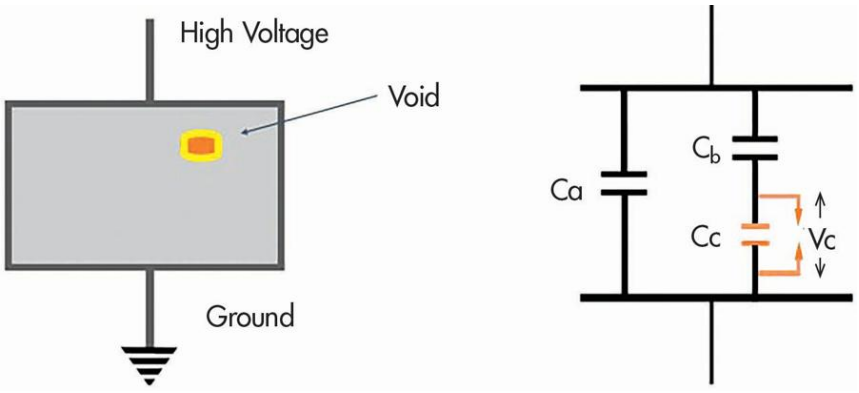

Figure 2. Physical schematic of a gas cavity contained within a solid insulator material and equivalent circuit model with three capacitors used for analysis of the partial discharge mechanism.

The capacitances for solid insulator and cavity are defined as follows:

$$C_a = \varepsilon_0 \varepsilon_{rm} \frac{A}{d_a} \quad (1)$$

$$C_a = \varepsilon_0 \varepsilon_{rc} \frac{A}{d_c} \quad (2)$$

Here, ε0 is the electrical permittivity of the cavity, εra is the relative dielectric constant of the solid insulator, ε_{rv} is the relative dielectric constant of the cavity, A is the surface area, da is the insulator thickness, and dc is the gap thickness.

In this capacitive structure connected in series, the voltage drop over the cavity is expressed as: (3)

$$V_c = V \frac{C_a}{C_a + C_c}$$

When this expression is written in terms of relative dielectric constants:

(4)

$$V_c = V \frac{\varepsilon_{ra}\, d_c}{\varepsilon_{ra}\, d_c + \varepsilon_{rc}\, d_a}$$

The electric field strength in the vacuum is:

(5)

$$E_c = \frac{V_c}{d_c}$$

It is defined as. As can be seen, $\varepsilon_{rm} \gg \varepsilon_{rv}$the electric field in the cavity increases significantly and this causes the partial discharge initial voltage to decrease. Therefore, the gap geometry and relative dielectric constant difference in solid insulators are among the key determinants of the partial discharge formation mechanism.

3. SRR-Based Microwave Sensor Design

Due to their advantages such as design flexibility, ease of fabrication, and high detection sensitivity, the use of microstrip-based microwave sensors is becoming increasingly common in the literature and industrial applications (Chowdhury et al., 2024; Han, Liu, & Zhang, 2024). In this study, a Slit Ring Resonator (SRR) structure and transmission line-based microwave sensor design was carried out in order to detect air gaps formed as a result of physical damage to medium and high voltage cable insulators with high precision. The proposed sensor is a two-port passive microwave circuit.

In the proposed sensor design, it is critical to transmit microwave signals with minimal loss and avoid reflections caused by impedance mismatch in the input-output ports of the system. For this purpose, the characteristic impedance of the sensor's supply lines is designed to be Z0 = 50 ohms. Electromagnetic wave propagation in microstrip transmission lines occurs in Quasi-TEM mode due to the boundary conditions between the dielectric substrate and the air environment. In the said mode, the conductive strip dimensions must be calculated by considering the thickness of the dielectric material and the relative dielectric constant (Ɛ') to obtain the targeted characteristic impedance value (Z_0). Equation 1 can be calculated and the electrical length, which depends on the effective dielectric constant, can be calculated by Equation 6 (Haque et al., 2022).

$$W = \frac{c}{2f_r}\sqrt{\frac{2}{\varepsilon_r + 1}} \quad (6)$$

$$L = \frac{c}{2f_r\sqrt{\varepsilon_{eff} + 1}} - 2\Delta L \quad (7)$$

$$\Delta L = 0{,}412h\frac{\varepsilon_{eff}+0{,}3}{\varepsilon_{eff}-0{,}258}\left[\frac{\frac{W}{h}+0{,}264}{\frac{W}{h}+0{,}8}\right]^{-\frac{1}{2}} \quad (8)$$

$$\varepsilon_{eff} = \frac{\varepsilon_r+1}{2}+\frac{\varepsilon_r-1}{2}\left[1+12\frac{h}{W}\right] \quad (9)$$

The impedance of the lines feeding the microstrip structures can be calculated by Equation 10.

$$Z_{giriş} = \frac{120\pi}{\sqrt{\epsilon_r}\left[\frac{h}{W}+1{,}393+0{,}667\ln\left(\frac{h}{W}+1{,}444\right)\right]} \quad (10)$$

Specified in Equations 5 and 6, it specifies the thickness of the dielectric material, the speed at which light travels in a vacuum, the resonant frequency, and the relative permittivity (dielectric constant) of the dielectric material. After determining the physical parameters that ensure impedance matching, the operating frequency of the sensor, which forms the basis of the detection mechanism, must be modeled theoretically. In this context, the resonant frequency of the designed microwave sensor is expressed by Equation 11 based on the equivalent LC circuit model of the structure:

$$f_r = \frac{1}{2\pi\sqrt{LC}} \quad (11)$$

The sensor's resonant frequency is determined by the geometric dimensions of the conductive rings that make up the resonator structure. The geometric parameters involved are fundamental elements that directly influence the total inductance and capacitance of the circuit. Thus, the parameters L and C in Equation 11 represent the equivalent inductance and capacitance of the sensor structure, respectively (Al-Mudhafar & Ra'ed, 2022).

In line with the theoretical background and design equations presented above, Arlon AD255C was preferred as the dielectric substrate of the proposed sensor due to its high frequency stability and low dielectric loss properties. Physical and electrical parameters of the material used in the design; The relative dielectric constant is 2.55, the loss tangent is 0.0014, the material thickness (h) is 0.728 mm, and the copper conductor thickness (t) is 35 µm. Examining the sensor geometry presented in Figure 3, it is seen that the structure consists of concentric ring resonators fed by microstrip transmission lines with a characteristic impedance of 50 Ω. The geometric parameters of the design, especially ring widths and capacitive cavities, are optimized to provide the targeted resonant frequency.

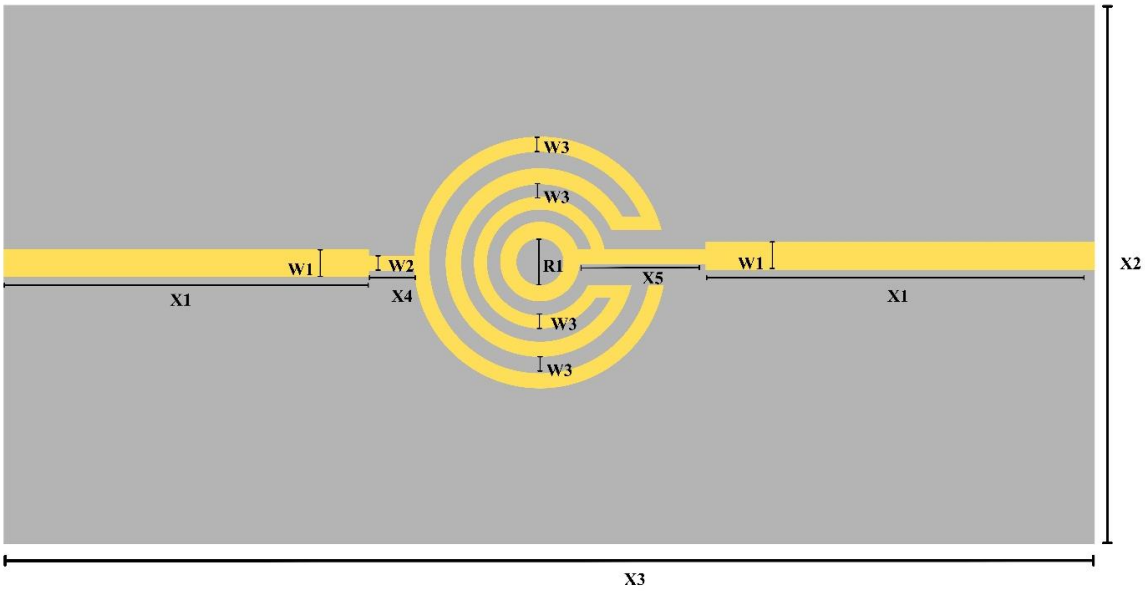

Figure 3. Geometric structure and sizing parameters of sensor design

The physical dimensions of the microwave sensor, whose schematic representation is given in Figure 3, were determined because of comprehensive parametric analysis and optimization processes carried out in the CST Microwave Studio environment. An SRR-based sensor consisting of helical structures has been proposed to concentrate the electric field at a specific central point to better detect cavities. While determining the operating frequency of the sensor, first, care was taken to ensure that the operating frequencies of the spectrum analyzer were between 0-6 GHz. While determining the sensor dimensions, the air gaps to be measured and the width of the slits were taken into consideration. In addition, with the parametric analyzes made during the sensor design phase, the sensitivity of the sensor at the frequency of 4.88 GHz was found to be sufficient. The SRR structure in the proposed sensor consists of intertwined, circular and interconnected discrete rings. The structure of these split rings determines the sensor's resonant frequency. The final geometric parameters that will provide the target resonance frequency of the sensor have been determined because of extensive optimization processes. The numerical values of these parameters are given collectively in Table 1.

Table 1. Values of the design parameters of the proposed sensor

Parameters	Value (mm)	Parameters	Value (mm)
X1	35.85	W1	1.80
X2	60	W2	0.50
X3	80	W3	0.50
X4	0.51	R1	0.40
X5	3.55		

When the data in the table are examined; The radius (R1) of the inner ring in the center of the resonator structure was determined as 1.5 mm and the conductor strip widths determining the capacitive coupling between the rings were determined as 0.5 mm. This geometric configuration ensures maximum concentration of the electric field in the sensor center, enabling the high sensitivity required for detecting deformations in the XLPE insulator. In line with the optimal geometric parameters determined because of numerical analysis, the prototype production of the microwave sensor was carried out. 50Ω SMA connectors were soldered to the input and output ports of the produced sensor to minimize signal transmission losses and made ready for measurement. The photograph of the prototype sensor is presented in Figure 4.

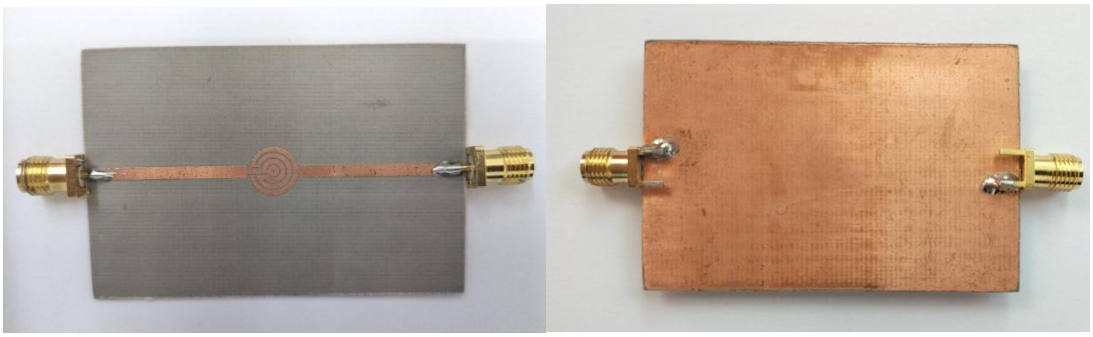

Figure 4. Front and back surfaces of the designed SRR-based microwave sensor

Following the manufacturing phase, S-parameters were examined both in a simulation environment and experimentally to verify the electromagnetic performance of the designed sensor and analyze its resonance characteristics. The electromagnetic performance of the SRR-based microwave sensor, whose design and production has been completed; S-parameters and electric field distribution at resonance frequency. As shown in Figure 5, the concentration level of the electric field and current distribution on the resonator, which is the main element determining the detection sensitivity of the sensor, was analyzed at a resonant frequency of 4.88 GHz when the sensor was unloaded (empty).

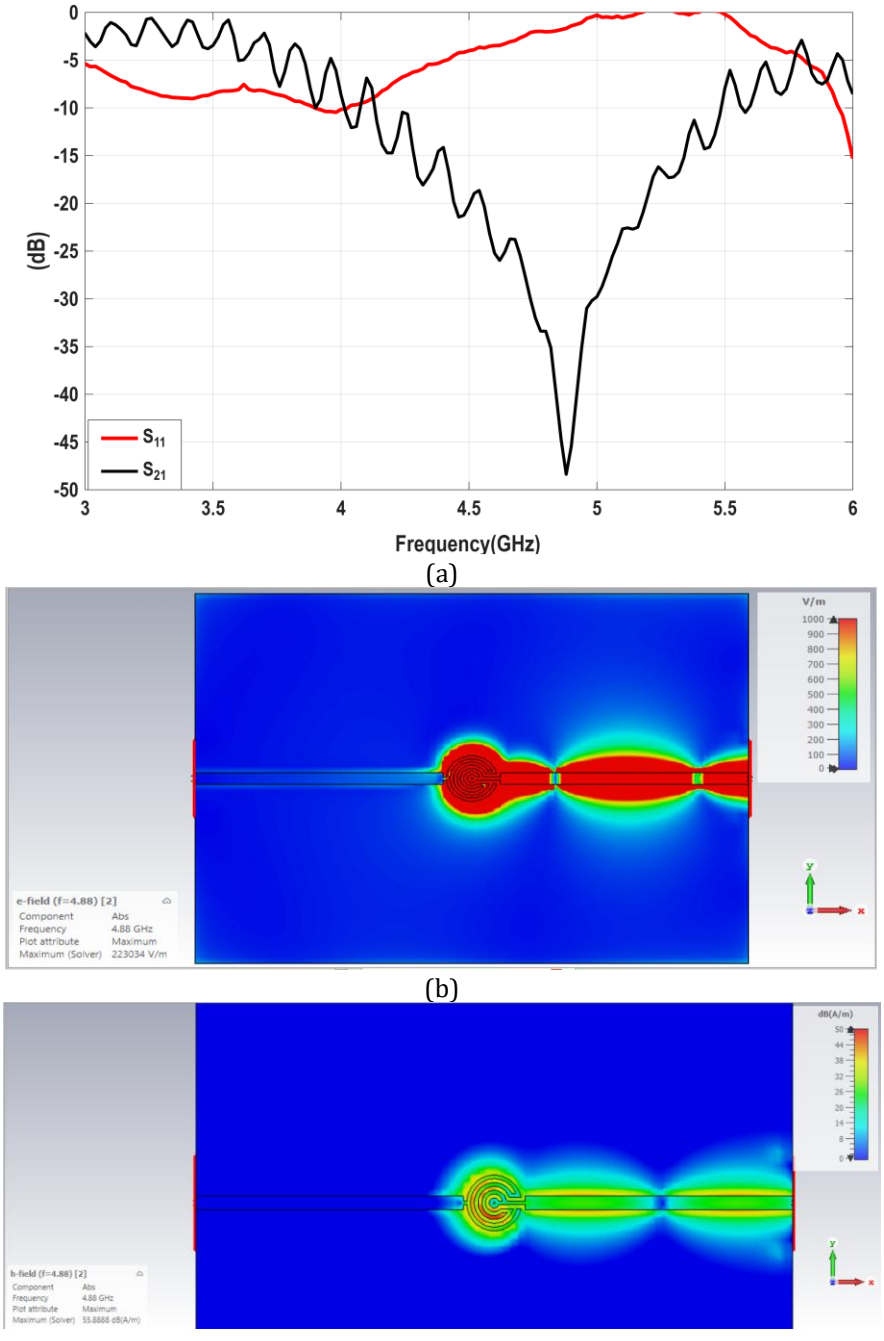

Figure 5. S-parameter results of the sensor (a), E-field distribution (b) and Current distribution (c) at resonant frequency

When the graph is examined, it is seen that there is a significant resonance in the S_{21} parameter of the sensor at 4.88 GHz. If the S_{11} value approaches 0 dB in the same frequency region, it indicates that the signal is largely reflected. The electric field distribution in Figure 5 reveals that the field is particularly concentrated at the center of the intertwined rings and in capacitive spaces. The current distribution on the sensor given in Figure 5 c appears to be concentrated in the resonator region.

To express the resonance characteristics and electromagnetic interactions in the physical structure of the proposed SRR-based microwave sensor with electrical parameters, an equivalent circuit model with bulk elements was created.

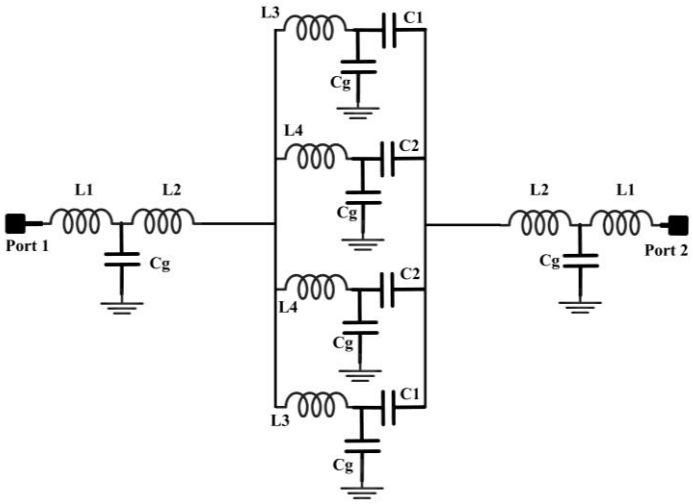

Figure 6. Electrical equivalent circuit model of the designed SRR-based microwave sensor

The equivalent circuit model with bulk elements created for the designed SRR-based microwave sensor includes the inductance and capacitance components of the resonator. The compatibility of circuit simulations performed in ADS with CST electromagnetic analyses confirms the accuracy of the equivalent circuit model. The sensor geometry was determined by parametric optimization in the CST environment. The L and C values in the equivalent circuit of the proposed sensor were obtained by optimization in the ADS simulation program. Finally, the final physical dimensions of the sensor and the associated RLC circuit elements that provide optimal performance at 4.88 GHz are presented in Table 2.

Table 2. Values of equivalent circuit parameters of the proposed sensor

Parameters	Value	Parameters	Value
L1	0.01 nH	C1	5.540 pF
L2	1.20 nH	C2	0.509 pF
L3	2.55 nH	Cg	1.75 pF
L4	0.05 nH		

In order to verify the validity of the geometric and electrical parameters given in Table 2; The results of the full-wave simulation conducted in the CST Microwave Studio, the outputs of the RLC equivalent circuit model obtained in the ADS environment, and the experimental measurements performed with the Rohde & Schwarz FSH6 Spectrum Analyzer were examined comparatively.

In the analysis of two-port microwave circuits, various parameter sets are used to describe the electrical relationship between the input and output ports. In this study, ABCD (transfer) parameters were preferred because they enable easy mathematical modeling of cascade (chain) connected structures. The expression given in equation (12) shows the basic ABCD parameter definition between the input and output ports in a two-port circuit.

$$\begin{bmatrix} V_1 \\ I_1 \end{bmatrix} = \begin{bmatrix} A & B \\ C & D \end{bmatrix} \begin{bmatrix} V_2 \\ I_2 \end{bmatrix} \tag{12}$$

ABCD parameters allow the entire circuit to be expressed with a single transfer matrix by directly associating the voltage and current values at the input port with their counterparts at the output port. The microwave sensor structure discussed in this study consists of three basic sub-blocks: input transmission line, central SRR resonator block and output transmission line. Equality (13) shows that the total ABCD matrix of the sensor is obtained by multiplying the ABCD matrices of the input line, center resonator block, and output line.

$$\begin{bmatrix} A_{\text{total}} & B_{\text{total}} \\ C_{\text{total}} & D_{\text{total}} \end{bmatrix} = \begin{bmatrix} A_{\text{in}} & B_{\text{in}} \\ C_{\text{in}} & D_{\text{in}} \end{bmatrix} \cdot \begin{bmatrix} A_{\text{center}} & B_{\text{center}} \\ C_{\text{center}} & D_{\text{center}} \end{bmatrix} \cdot \begin{bmatrix} A_{\text{out}} & B_{\text{out}} \\ C_{\text{out}} & D_{\text{out}} \end{bmatrix} \tag{13}$$

One of the key advantages of ABCD parameters is that the total transfer matrix in cascade-coupled circuits can be

calculated by multiplying the ABCD matrices of the subblocks. Thanks to this feature, complex structures can be divided into simpler subblocks and modeled systematically and analytically. In the proposed sensor structure, the input and output transmission lines are symmetrical. Hence the ABCD matrices of both lines have the same mathematical form and are defined only by physical length parameters. This approach maintains both the physical significance and mathematical simplicity of the model. In equations (14)– (15), the ABCD parameters of the input and output transmission lines are given.

$$\begin{bmatrix} A_{\text{in}} & B_{\text{in}} \\ C_{\text{in}} & D_{\text{in}} \end{bmatrix} = \begin{bmatrix} \cos(\beta l_{\text{in}}) & jZ_0 \sin(\beta l_{\text{in}}) \\ j\frac{1}{Z_0}\sin(\beta l_{\text{in}}) & \cos(\beta l_{\text{in}}) \end{bmatrix} \tag{14}$$

$$\begin{bmatrix} A_{\text{out}} & B_{\text{out}} \\ C_{\text{out}} & D_{\text{out}} \end{bmatrix} = \begin{bmatrix} \cos(\beta l_{\text{out}}) & jZ_0 \sin(\beta l_{\text{out}}) \\ j\frac{1}{Z_0}\sin(\beta l_{\text{out}}) & \cos(\beta l_{\text{out}}) \end{bmatrix} \tag{15}$$

The phase constantly given in the relevant equations $\beta = \frac{2\pi}{\lambda}$ is given by characteristic impedance. Also $Z_0 l_{\text{out}} = l_{\text{in}}$, their values are equal. The central resonator block is the fundamental structure that determines the sensor's frequency selectivity and resonance behavior. Each SRR arm creates a strong resonance at a certain frequency, changing the amplitude and phase characteristics of the signal in the transmission line. In terms of physical layout, these four parallel arms behave as if they are connected in series to the transmission line. Series inductance, Shunt capacitance, Series capacitance matrices are given by equations 16, 17 and 18.

$$\begin{bmatrix} 1 & j\omega L_3 \\ 0 & 1 \end{bmatrix} \tag{16}$$

$$\begin{bmatrix} 1 & 0 \\ j\omega C_g & 1 \end{bmatrix} \tag{17}$$

$$\begin{bmatrix} 1 & \frac{1}{j\omega C_1} \\ 0 & 1 \end{bmatrix} \tag{18}$$

Type-1 and Type-2 arms are modeled separately because they have different inductance and capacitance values. The ABCD matrix for each branch was obtained by multiplying the transfer matrices of the series and shunt elements in accordance with the physical order of the circuit elements. This method provides a direct relationship between the physical structure of the SRR and the mathematical model. Equations (19) and (20) show the ABCD matrices of the Type-1 and Type-2 SRR arms.

$$T_{\text{arm1}} = \begin{bmatrix} 1 & j\omega L_3 \\ 0 & 1 \end{bmatrix} \begin{bmatrix} 1 & 0 \\ j\omega C_g & 1 \end{bmatrix} \begin{bmatrix} 1 & \frac{1}{j\omega C_1} \\ 0 & 1 \end{bmatrix} \tag{19}$$

$$T_{\text{arm2}} = \begin{bmatrix} 1 & j\omega L_4 \\ 0 & 1 \end{bmatrix} \begin{bmatrix} 1 & 0 \\ j\omega C_g & 1 \end{bmatrix} \begin{bmatrix} 1 & \frac{1}{j\omega C_2} \\ 0 & 1 \end{bmatrix} \tag{20}$$

The SRR arms in the central resonator block are connected parallel to each other. Admittance (Y) parameters were used to calculate the total effect of these structures. Therefore, the ABCD matrix of each SRR arm was first converted to admittance parameters, and then the total admittance of the parallel arms was calculated. The transformation expressions given in equation (21-24) are the standard relations used to transition from ABCD parameters to Y-parameters.

$$Y_{11} = \frac{D}{B} \tag{21}$$

$$Y_{12} = \frac{AD - 1}{B} \tag{22}$$

$$Y_{21} = -\frac{1}{B} \tag{23}$$

$$Y_{22} = \frac{A}{B} \tag{24}$$

The central resonator block was formed by connecting two Type-1 and two Type-2 SRR arms in parallel. The total admittance of the parallel-connected structures is obtained as the algebraic sum of the admittance of each arm. Accordingly, the total admittance matrix of the central resonator block is defined in equations (25-26). This step makes it possible to represent the multi-arm resonator structure with a single set of equivalent parameters.

$$Y_{\text{total}} = Y_1 + Y_2 + Y_3 + Y_4 \tag{25}$$

$$Y_{\text{center}} = 2Y_{\text{arm1}} + 2Y_{\text{arm2}} \tag{26}$$

After obtaining the total admittance of the parallel SRR arms, the equivalent impedance of the central resonator block connected in series to the transmission line was calculated. This impedance was defined over the input admittance of the total admittance matrix. This approach allows the center resonator block to behave as a single frequency-dependent series impedance element at the system level, providing a model consistent with transmission line theory.

$$Z_{\text{center}} = \frac{1}{Y_{\text{center},11}} \tag{27}$$

Since the central resonator block is modeled as a serial impedance, the ABCD matrix of this block is reduced to a fairly simple form. The transfer matrix given in equation (28) represents the effect of the central resonator block on the transmission line in a clear and physically significant way.

$$\begin{bmatrix} A_{\text{center}} & B_{\text{center}} \\ C_{\text{center}} & D_{\text{center}} \end{bmatrix} = \begin{bmatrix} 1 & Z_{\text{center}} \\ 0 & 1 \end{bmatrix} \tag{28}$$

The input transmission line and the central resonator block were connected in cascade, and an intermediate ABCD matrix was obtained. Then, this intermediate matrix was multiplied by the ABCD matrix of the output transmission line and the total ABCD matrix of the system was calculated. The parameters A_{total}, B_{total}, C_{total}, D_{total} obtained in this phase represent the entire electromagnetic behavior of the sensor as a single two-port circuit.

$$\begin{bmatrix} A_1 & B_1 \\ C_1 & D_1 \end{bmatrix} = \begin{bmatrix} A_{\text{in}} & B_{\text{in}} \\ C_{\text{in}} & D_{\text{in}} \end{bmatrix} \cdot \begin{bmatrix} 1 & Z_{\text{center}} \\ 0 & 1 \end{bmatrix} \tag{29}$$

$$\begin{aligned} A_1 &= A_{\text{in}} \\ B_1 &= A_{\text{in}} Z_{\text{center}} + B_{\text{in}} \\ C_1 &= C_{\text{in}} \\ D_1 &= C_{\text{in}} Z_{\text{center}} + D_{\text{in}} \end{aligned} \tag{30}$$

$$\begin{bmatrix} A_{\text{total}} & B_{\text{total}} \\ C_{\text{total}} & D_{\text{total}} \end{bmatrix} = \begin{bmatrix} A_1 & B_1 \\ C_1 & D_1 \end{bmatrix} \cdot \begin{bmatrix} A_{\text{out}} & B_{\text{out}} \\ C_{\text{out}} & D_{\text{out}} \end{bmatrix} \tag{31}$$

The parameters A_{total}, B_{total}, C_{total}, D_{total} used in the transformation expressions given in equations (32) are the ABCD parameters of the whole system.

$$\begin{aligned} A_{\text{total}} &= A_{\text{in}}A_{\text{out}} + (A_{\text{in}}Z_{\text{center}} + B_{\text{in}})C_{\text{out}} \\ B_{\text{total}} &= A_{\text{in}}B_{\text{out}} + (A_{\text{in}}Z_{\text{center}} + B_{\text{in}})D_{\text{out}} \\ C_{\text{total}} &= C_{\text{in}}A_{\text{out}} + (C_{\text{in}}Z_{\text{center}} + D_{\text{in}})C_{\text{out}} \\ D_{\text{total}} &= C_{\text{in}}B_{\text{out}} + (C_{\text{in}}Z_{\text{center}} + D_{\text{in}})D_{\text{out}} \end{aligned} \quad (33)$$

The parameters that can be measured directly in microwave measurement systems are S-parameters. Therefore, the theoretically obtained ABCD parameters need to be converted to S-parameters in order to be compared with experimental data. S-Parameter transformations are given in equations (34-35).

$$S_{11} = \frac{A_{\text{total}} + \frac{B_{\text{total}}}{Z_0} - C_{\text{total}}Z_0 - D_{\text{total}}}{A_{\text{total}} + \frac{B_{\text{total}}}{Z_0} + C_{\text{total}}Z_0 + D_{\text{total}}} \quad (34)$$

$$S_{21} = \frac{2}{A_{\text{total}} + \frac{B_{\text{total}}}{Z_0} + C_{\text{total}}Z_0 + D_{\text{total}}} \quad (35)$$

And values obtained as a result of this conversion directly reveal the reflection and transmission characteristics of the sensor (Ebrahimi & Ghorbani, 2023),(Pozar,2011).
"The transmission coefficient S_{21} frequency responses obtained from theoretical calculation, equivalent circuit, simulation, and experimental measurement methods are presented comparatively in Figure 7.

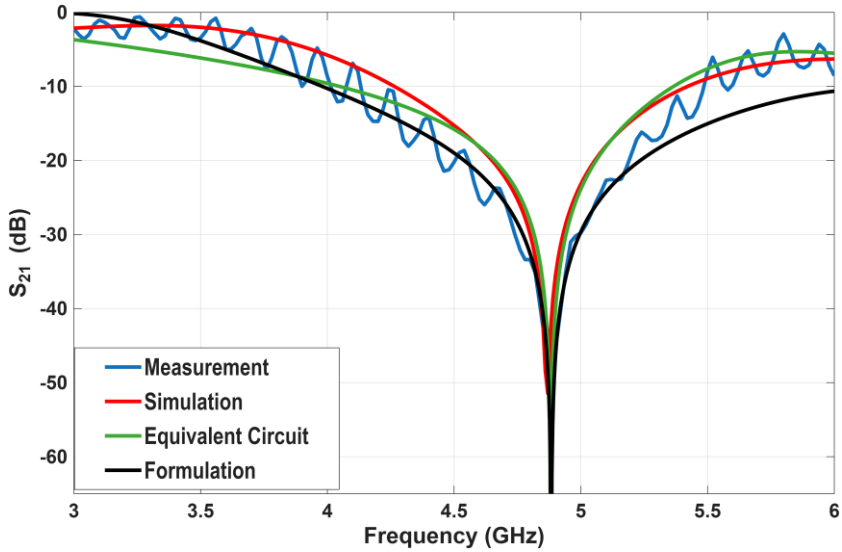

Figure 7. Comparison of simulation, measurement, and theoretical circuit analysis data verifying the resonant performance of the proposed structure.

Examining Figure 7, it is seen that both the CST simulations and the equivalent circuit model create a distinct and coherent resonance trough at the center frequency of 4.88 GHz. This agreement shows that the developed RLC model accurately represents the inductive and capacitive interactions in the sensor's physical structure. Partial incompatibility occurred between simulation, equivalent circuit and measurement results. These incompatibilities may be caused by printing errors, SMA connector effects, and cable losses that occur during the printing circuit of the sensor.

4. XLPE Insulator surface defect formation and Measurement Setup

A controlled measurement environment was created to experimentally verify the performance of the designed SRR-based microwave sensor in detecting insulation defects in medium voltage cables. In this context, artificial surface defects were created on a real XLPE cable sample that simulate physical damage that may occur under operating conditions, and the sensor's resonance responses to these defects were analyzed. Measurement station used in experimental studies consists of a spectrum analyzer capable of precise S-parameter measurement, a data acquisition unit and a sensor structure integrated into the test sample. To minimize the effect of environmental

noise during measurements and to ensure the stability of the contact between the sensor and the cable surface, the sensor is fixed on the cable. The general view and components of the experimental measurement setup are presented in Figure 8.

Figure 8. Experimental measurement setup and test environment where performance analysis of the designed microwave sensor is carried out

As seen in Figure 8, the input and output ports of the sensor were connected to the Rohde & Schwarz FSH6 model spectrum analyzer via low-loss coaxial cables with phase stability, and the data obtained were simultaneously transferred to the computer environment. In the transmission coefficient (S21) measurements of the microwave sensor, Mini-Circuits brand FL141-24SM+ model cables operating at DC-18 GHz frequency were used. The periodic ripples observed in these measurements are standing wave effects caused by inevitable impedance discontinuities between cables, connectors, and device interfaces in the measurement setup. These fluctuations correlate with the calibration tolerances and system noise floor of the spectrum analyzer used. These parasitic effects do not change the basic performance parameters of the sensor, such as resonance frequency and sensitivity, and should be considered as a characteristic behavior of the measurement system. In the measurement setup, XLPE insulated power cable, which is widely used in medium voltage distribution networks, was preferred as the sample to test the detection performance of the sensor. The basic layer structure and cross-sectional view of the cable sample used in experimental studies are given in Figure 9.

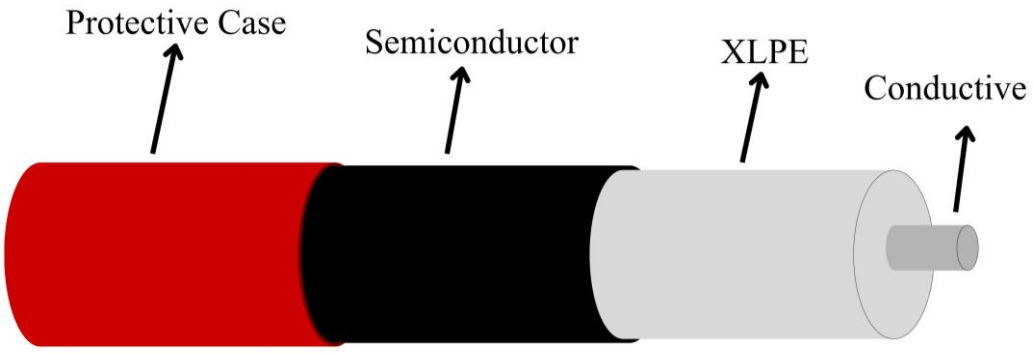

Figure 9. General layer structure of XLPE cable used as test specimen

When Figure 9 is examined; It is seen that the current carrier conductor is in the center, there are semiconductor layers on this conductor that homogenize the electric field distribution, and the main insulation is provided by the XLPE (Cross-Linked Polyethylene) layer. The focus in this study is on the XLPE insulator layer, where dielectric strength is most critical. To analyze the sensitivity of the designed microwave sensor to air gaps of different geometry and depth on the insulating material, controlled physical deformations were created on the cable sample. In this context, in addition to the "Non-Damaged" reference case, three different defect scenarios (Case 1, Case 2 and Case 3) representing damage in different parts of the insulator were designed. The schematic representation of the prepared test scenarios is presented in Figure 10.

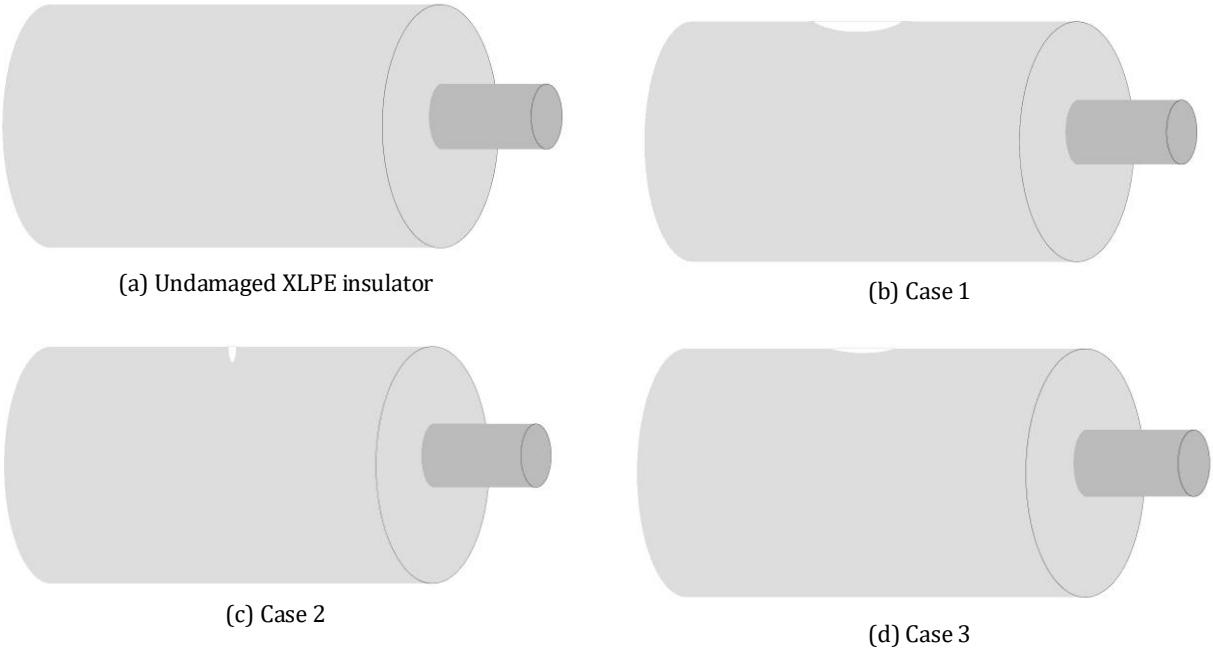

(a) Undamaged XLPE insulator (b) Case 1

(c) Case 2 (d) Case 3

Figure 10. Classification of artificial defect geometries modeled on the XLPE insulator layer: (a) Perfect reference structure, (b) Cavity with high volumetric and radial depth, (c) Narrow cavity advanced on the vertical axis, (d) Cavity with high lateral width but low depth.

When the physical properties of the scenarios presented in Figure 10 were examined, a reference measurement was first made on the undamaged XLPE insulator to determine the resonance frequency of the sensor. Following this reference; Case 1 scenarios representing large volume internal cavities, Case 2 representing deep and localized damage caused by cutting tools, and Case 3 scenarios representing shallow deformations such as superficial wear or stripping were created. For each scenario, the sensor was integrated into the cable surface and the transmission parameter (S_{21}) was measured; The resonance frequency shifts caused by the damaged conditions relative to the reference were evaluated comparatively.

5. Measurement Results of XLPE Air Void

To evaluate the performance of the designed microwave sensor in detecting defects of different types and depths in the XLPE cable insulator, extensive experimental measurements were carried out on the three different failure scenarios (Case 1, Case 2, and Case 3) identified earlier. Within the scope of the study, four different configurations were analyzed to determine how the detection sensitivity of the sensor is affected by the presence of cable layers: 'XLPE' only, where the sensor directly touches the insulator surface, 'XLPE + Outer Sheath' with a protective sheath on the insulator, 'XLPE + Semiconductor' with only the semiconductor layer included, and 'XLPE + Semiconductor + Outer Sheath', where the full cable structure is simulated. For each configuration, the transmission coefficient (S_{21}) frequency responses of the sensor were recorded and the measurement results obtained by examining the resonance frequency shifts relative to the undamaged reference state are presented in Figure 11.

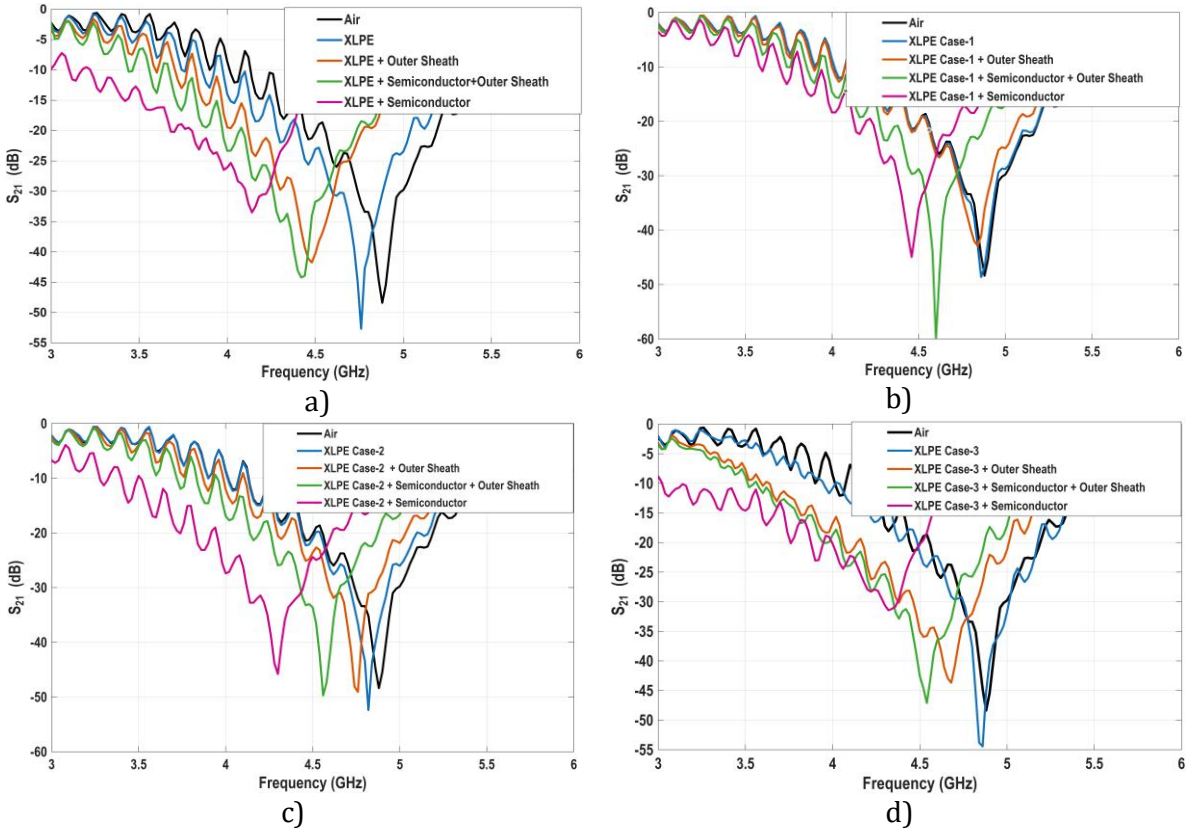

Figure 11. Geometric classification of XLPE cable insulation defects used in experimental analyses: (a) Perfect reference (base) structure, (b) Deformation with high radial depth and volume (Case-1), (c) Deep deformation with narrow cross-section advancing on the vertical axis (Case-2), (d) Deformation with a wide lateral surface but low penetration depth (Case-3).

When the graphical data presented in Figure 11 are analyzed, it is seen that significant changes occur in the resonance frequency of the sensor in all the defect scenarios constructed. Especially in the Case 1 scenario, where the air gap with a dielectric constant of about 1 is the largest in volume, significant deviations in the resonance frequency were recorded because of the change in the effective dielectric constant. While the idle frequency of the sensor is 4.88 GHz; only in the case of Case 1 damage on the XLPE insulator, the resonance frequency was measured as 4.86 GHz. In the full cable configuration, semiconductor and outer protective sheath layers are included in the cable structure, it was determined that the resonance frequency for Case 1 damage decreased to 4.60 GHz, although the distance between the sensor and the defective region increased. This data suggests that the sensor can detect not only the presence of a cavity but also the dielectric charging effect brought about by the layers with precision. As seen in Figure 10(c), even in a full cable configuration, the sensor can detect shallow damages represented by Case 3 with a sensitivity of 4.54 GHz MHz. Furthermore, the differentiation of frequency responses for Case 2, which represents narrow and deep damage, and Case 3, which represents wide and shallow damage, reveals that the sensor has the potential to distinguish the geometric structure of the defect. The results obtained prove that the proposed SRR-based sensor design has sufficient sensitivity to detect cable defects even in the presence of protective layers.

To comprehensively analyze the performance of the designed microwave sensor in detecting different cable defects, each damage scenario (Case 1, Case 2, Case 3) was tested separately under different layer configurations of the cable. This approach is designed to determine whether the sensor maintains its detection sensitivity not only on the bare insulator but even in the presence of additional layers such as the semiconductor layer and protective outer sheath. The obtained experimental S21 results are grouped according to the effect of the cable layers and presented in Figure 12.

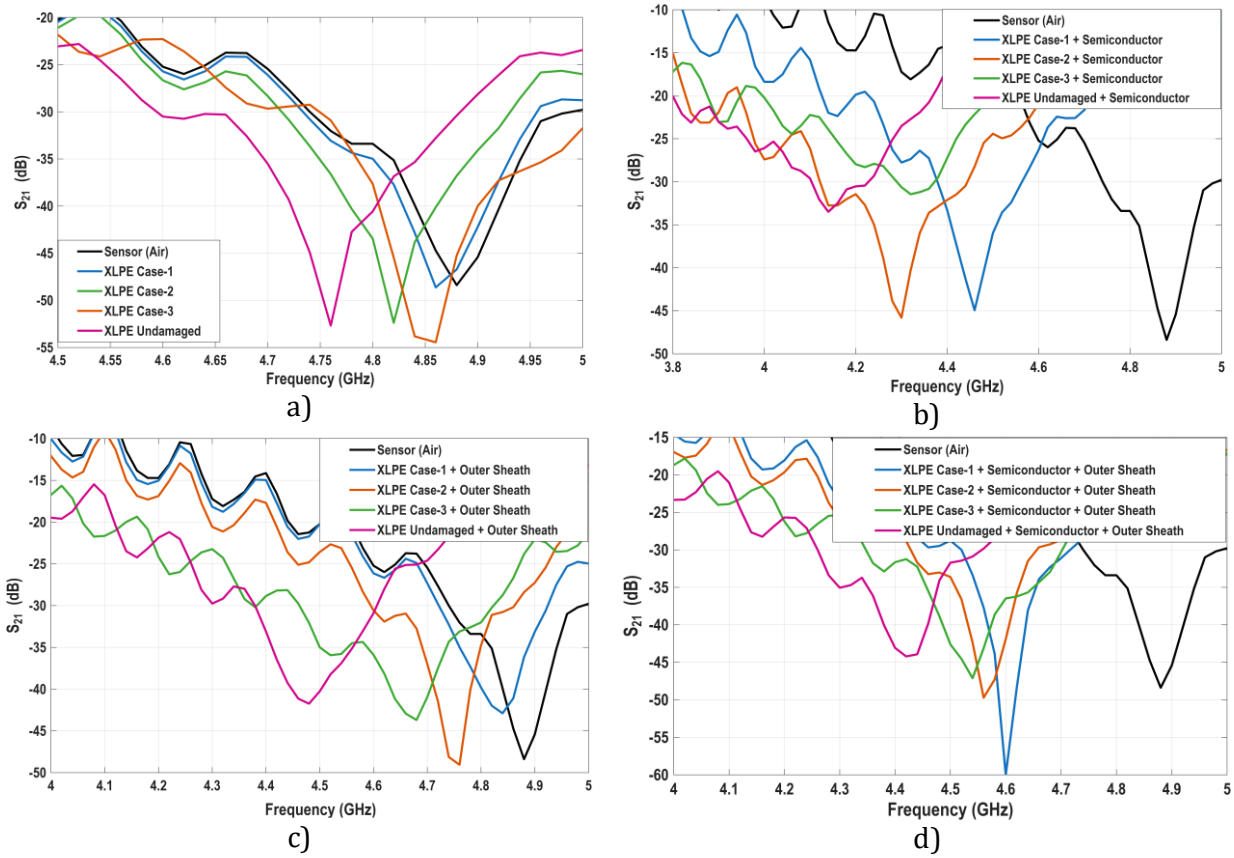

Figure 12. Comparative spectral analysis of the generated damage scenarios (Cases-1, 2, 3) with the perfect reference state in the presence of different cable layers: (a) Flaw detection only on the XLPE insulator, (b) Frequency responses of the defects when the semiconductor layer is added, (c) Effect of the outer sheath on defect signals without a semiconductor, (d) Final comparison of damage and reference states in the complete cable structure.

Measurements with the proposed sensor have been validated with at least three repetitions. Measurement Results show high repeatability. The measurement results are shown in Figure 12. It is seen that significant variations occur in the sensor's resonance frequency in all layer configurations considered, depending on the defect type. Within the scope of the analyses, the 'XLPE Insulator Only' condition (Figure 11 (a)), which is the ideal measurement condition where the sensor directly touches the damaged surface, was examined. In this configuration, a maximum shift in the resonant frequency of approximately 120 MHz was recorded, especially in case 1 scenario, which stands out for its volumetric magnitude. The detection of distinguishable frequency variations in the Case 2 and Case 3 scenarios compared to the reference (undamaged) state proves that the sensor exhibits a high sensitivity to variations in cavity volume.

When the case where a semiconductor layer with conductive characteristics is added to the insulator (Figure 11b) is analyzed, it is seen that in the Case 2 scenario, which is a deeply penetrating damage type, the defect can be clearly detected despite the shielding effect of the semiconductor layer.
When the measurement results (Figure 11(c)) of the 'XLPE + Outer Sheath' configuration, in which the protective sheath, which is the outermost layer of the cable, is passed over the perfect XLPE and damaged samples (Cases 1, 2, 3) are examined; The resonant frequency of the referenced perfect sample was recorded as 4.48 GHz. In the damage analysis carried out under the same configuration; It was determined that the resonance frequency increased to 4.84 GHz in the Case 1 scenario, where the volumetric gap was most pronounced, and in the Case 2 and Case 3 scenarios, resonance occurred at 4.76 GHz and 4.68 GHz, respectively. Although the protective sheath layer between the sensor and the defective area tends to weaken the coupling effect by increasing the physical distance, the significant frequency differences achieved prove that the sensor can distinguish air gaps in the inner insulator with high precision, even though the outer sheath.

Analyzing the Figure 12(d) graph, which most realistically reflects the field conditions and simulates the full cable structure (XLPE + Semiconductor + Outer Sheath), critical findings about the performance of the sensor were reached. While the resonance frequency was measured as 4.42 GHz in the referenced perfect full cable structure; With the effect of defects created in the insulator layer, significant upward shifts occurred in this frequency. In the Case 1 scenario, where the volumetric air gap is the widest, the resonance frequency increased to 4.60 GHz; In the State 2 and State 3 scenarios, values of 4.56 GHz and 4.54 GHz were recorded, respectively. Despite the cable's

protective layers, such as the semiconductor and outer sheath, these significant frequency variations confirm that the designed sensor's electromagnetic penetration depth is capable of detecting gaps in the inner insulator (XLPE) beyond the outer layers. In the light of all these experimental data obtained; it is concluded that the proposed SRR-based sensor design has the potential to detect insulation defects with high accuracy without stripping the protective layers on the cable and without causing any physical damage to the system.

Table 3 below summarizes the resonant frequencies and frequency variations of the designed sensor under idle conditions (air), on a reference cable (perfect full cable), and across different damage scenarios (Case 1, Case 2, and Case 3). These measurements were conducted to verify the sensor's response to different media and its capability for damage detection.

Table 3. Resonant frequencies and frequency variations of the sensor in idle, reference cable and different damage scenarios

Measurement Status	Resonant Frequency (f_r) [GHz]	Frequency Shift (Δf) [MHz]
Sensor (Air)	4.88	-
Case 1	4.60	280
Case 2	4.56	320
Case 3	4.54	340
Reference (Perfect Full Cable)	4.42	460

Examining the data in Table 3, it is observed that the sensor has a resonant frequency of 4.88 GHz in the idle state (air). When placed on the reference (intact) cable, which has a higher dielectric constant than air, the resonant frequency shifts down to 4.42 GHz, resulting in a maximum frequency shift of 460 MHz. In the different damage scenarios (Case 1, 2, and 3), the resonant frequencies are observed to vary between 4.60 GHz and 4.54 GHz. This indicates that air voids or deformations in the damaged areas alter the effective permittivity, causing the resonant frequency to shift upwards compared to the reference cable. Consequently, the sensor effectively distinguishes between the healthy cable and various defect types through distinct differences in frequency shifts.

A comparative analysis of the characteristic features of various UHF sensor designs developed for partial discharge detection in the literature and the sensor structure proposed in this study is presented in Table 4.

Table 4. Comparison of proposed UHF sensor designs for PD detection.

Reference	Type	Frequency Range	S-Parameter
(SikorSki et al., 2018)	Fractal Antenna	0.8–2 GHz	S_{11}
(Zhang et al., 2017)	Antipodal Vivaldi Antenna	0.8–3 GHz	S_{11}
(Xavier et al., 2019)	Microstrip Antenna	0.3–1.5 GHz	S_{11}
(Li et al., 2012)	Log-Spiral antenna	0.7 GHz–3 GHz	S_{11}
(Rostaghi-Chalaki et al., 2020)	Cylinder Transmission Line	1,2 -1,4	S_{11}
(Yadam et al., 2022)	Archimedes Spiral Antenna	0.5–5 GHz	S_{11}
This study	CSRR-Based Transmission Line	4.88-4.42	S_{21}

Upon examining Table 4, it is observed that existing studies in literature predominantly focus on detecting discharge signals using antenna-based structures via the reflection coefficient. In contrast, the SRR-based transmission line sensor proposed in this study distinguishes itself from the literature by offering a novel approach that detects air voids within the insulation—which predispose the system to discharge—before the discharge initiates, by monitoring variations in the transmission coefficient parameter.

5. Conclusion and Discussion

In this study, a SRR sensor design based on microwave resonance technique was carried out for the non-destructive detection of structural distortions in the insulator layer of high-voltage power cables and air gaps caused by partial discharge, and its performance was experimentally verified. The proposed sensor was developed with the aim of identifying air gaps that cause partial discharge, unlike antenna-based sensors commonly used in the literature that focus on detecting partial discharge formation. Antenna-based approaches are intended to detect partial discharge events by analyzing variations in the S_{11} reflection parameter. In contrast, the sensor presented in this study uses a transmission line-based architecture and aims to detect air gaps within the cable insulation through the S21 transmission parameter. Through this approach, the sensor can be used without any stress applied to the cable, offering a significant advantage for preventive maintenance applications by enabling the identification of potential defects before partial discharge occurs.

The developed sensor exhibited a high sensitivity to small volumetric changes in the dielectric medium. The air gaps in the insulator reduced the effective dielectric constant of the medium, causing significant upward shifts in the resonance frequency. In fact, the sensor's detection capability in the microwave region is demonstrated by recording a maximum frequency deviation of approximately 120 MHz compared to the reference state on the bare XLPE surface, which is the ideal measurement condition. As the most critical finding of the study, the sensor was able to successfully detect internal insulator defects despite the electrical shielding effect of the semiconductor layer and the physical distance created by the outer protective sheath. In the full cable structure (XLPE + Semiconductor + Outer Sheath) simulating field conditions, the resonance frequency, which was 4.42 GHz for the perfect reference situation, increased to 4.60 GHz in the scenario where the volumetric gap was most dominant. Distinguishable resonance variations have been achieved even with smaller volume defects, confirming that the sensor's penetration depth exceeds the outer layers and is sufficient to analyze the internal structure.

Furthermore, the direct proportional relationship between the amount of volumetric void and the frequency shift revealed that the sensor can be used to rate not only the presence of the defect, but also its magnitude and characteristic. Measurements can be performed instantaneously and rapidly in real-world systems using a vector network analyzer or a spectrum analyzer, and the sensor operates compatibly with these devices. However, the transportation and use of such analyzers in field conditions can pose practical difficulties; Their high cost can limit their effectiveness in field applications. Therefore, future studies aim to develop a more compact and portable measurement system where sensor outputs can be evaluated without the need for external analyzers. In this context, the presented study is a pioneer in terms of the development of integrated and practical sensor systems for real field applications.

Conflict of Interest

No conflict of interest was declared by the authors.

References

Al-Mudhafar, A. A., & Ra'ed, A. M. (2022). High-precise microwave active antenna sensor (MAAS) formulated for sensing liquid properties. Sensors and Actuators A: Physical, 341, 113567.

Arikan, O., Uydur, C. C., & Kumru, C. F. (2023). Insulation evaluation of MV underground cable with partial discharge and dielectric dissipation factor measurements. Electric Power Systems Research, 220, 109338.

Bartnikas, R. (2002). Detection of partial discharges (corona) in electrical apparatus. IEEE transactions on Electrical Insulation, 25(1), 111-124.

Bartnikas, R. (2002). Partial discharges. Their mechanism, detection and measurement. IEEE Transactions on Dielectrics and Electrical Insulation, 9(5), 763-808.

Chai, H., Phung, B. T., & Mitchell, S. (2019). Application of UHF sensors in power system equipment for partial discharge detection: A review. Sensors, 19(5), 1029.

Chimunda, S., & Nyamupangedengu, C. (2019). A reliability assessment model for an outdoor 88 kV XLPE cable termination. Electric Power Systems Research, 177, 105979.

Chowdhury, M. Z. B., Islam, M. T., Alzamil, A., Soliman, M. S., & Samsuzzaman, M. (2024). A tunable star-shaped highly sensitive microwave sensor for solid and liquid sensing. Alexandria Engineering Journal, 86, 644-662.

Densley, J. (2002). Ageing mechanisms and diagnostics for power cables-an overview. IEEE electrical insulation magazine, 17(1), 14-22.

Dissado, L. (2002). Understanding electrical trees in solids: from experiment to theory. IEEE Transactions on Dielectrics and Electrical Insulation, 9(4), 483-497.

Forssen, C., & Edin, H. (2008). Partial discharges in a cavity at variable applied frequency part 2: measurements and modeling. IEEE Transactions on Dielectrics and Electrical Insulation, 15(6), 1610-1616.

Genç, İ., Gözel, M. A., & Kahriman, M. (2025). Microwave sensor design with directional coupler-based CSRR structure for the characterization of the dielectric properties of solid materials. Measurement, 119548.

Gocen, C., & Palandoken, M. (2023). UHF RFID microwave sensor Tag design for an RSSI-Based machine learning assisted binary Ethanol–Water mixture characterization. IEEE Sensors Journal, 24(1), 262-269.

Gocen, C., & Palandoken, M. (2024). Equivalent Circuit Model of Two Symmetrical Split Ring Resonators based Microwave Sensor Design.

Han, X., Liu, K., & Zhang, S. (2024). High-sensitivity dual-band microfluidic microwave sensor for liquid dielectric characterization. IEEE Sensors Journal.

Han, X., Liu, K., Zhang, S., Peng, P., Fu, C., Qiao, L., & Ma, Z. (2024). CSRR metamaterial microwave sensor for measuring dielectric constants of solids and liquids. IEEE Sensors Journal, 24(9), 14167-14176.

Haque, M. A., Sarker, N., Sawaran Singh, N. S., Rahman, M. A., Hasan, M. N., Islam, M., Zakariya, M. A., Paul, L. C., Sharker, A. H., & Abro, G. E. M. (2022). Dual band antenna design and prediction of resonance frequency using machine learning approaches. Applied Sciences, 12(20), 10505.

Hossen, M. S., Islam, M. T., Alawad, M. A., Kirawanich, P., Baharuddin, M. H., Alkhrijah, Y., Ouda, M., & Soliman, M. S. (2025). Miniaturized Metamaterial Microwave Sensor with ML Assisted Optimization for Label-Free Liquid Sensing. IEEE Sensors Journal.

Illias, H., Chen, G., & Lewin, P. L. (2011). Modeling of partial discharge activity in spherical cavities within a dielectric material. IEEE electrical insulation magazine, 27(1), 38-45.

Islam, M. A., & Kharkovsky, S. (2016). Detection and monitoring of gap in concrete-based composite structures using microwave dual waveguide sensor. IEEE Sensors Journal, 17(4), 986-993.

Kaziz, S., Said, M. H., Imburgia, A., Maamer, B., Flandre, D., Romano, P., & Tounsi, F. (2023). Radiometric partial discharge detection: A review. Energies, 16(4), 1978.

Kiani, S., Rezaei, P., Navaei, M., & Abrishamian, M. S. (2018). Microwave sensor for detection of solid material permittivity in single/multilayer samples with high quality factor. IEEE Sensors Journal, 18(24), 9971-9977.

Kreuger, F., Gulski, E., & Krivda, A. (2002). Classification of partial discharges. IEEE transactions on Electrical Insulation, 28(6), 917-931.

Kumru, C. F., Lutfi, A., El-Hag, A., Darwish, A., Refaat, S. S., & Abu-Rub, H. (2023). A study on the ability of different non-intrusive sensors for diagnosing outdoor insulator defects. 2023 IEEE Electrical Insulation Conference (EIC),

Li, T., Rong, M., Zheng, C., & Wang, X. (2012). Development simulation and experiment study on UHF partial discharge sensor in GIS. IEEE Transactions on Dielectrics and Electrical Insulation, 19(4), 1421-1430.

Liu, M., Liu, Y., Li, Y., Zheng, P., & Rui, H. (2017). Growth and partial discharge characteristics of electrical tree in XLPE under AC-DC composite voltage. IEEE Transactions on Dielectrics and Electrical Insulation, 24(4), 2282-2290.

Niemeyer, L. (2002). A generalized approach to partial discharge modeling. IEEE Transactions on Dielectrics and Electrical Insulation, 2(4), 510-528.

Palandoken, M., & Gocen, C. (2025a). Microwave sensor designs for liquid material dielectric characterization: Technological advances and applications. Sensors and Actuators A: Physical, 116381.

Palandoken, M., & Gocen, C. (2025b). RFID-enabled ML-assisted microwave liquid sensor design for complex dielectric characterization of water-methanol mixture. Sensors and Actuators A: Physical, 382, 116142.

Palandoken, M., Gocen, C., Khan, T., Zakaria, Z., Elfergani, I., Zebiri, C., Rodriguez, J., & Abd-Alhameed, R. A. (2023). Novel microwave fluid sensor for complex dielectric parameter measurement of ethanol–water solution. IEEE Sensors Journal, 23(13), 14074-14083.

Pozar, D. M., Microwave Engineering. Hoboken, NJ, USA: Wiley, 2011

Rostaghi-Chalaki, M., Yousefpour, K., Donohoe, J. P., Kurum, M., Park, C., & Klüss, J. (2020). Design of transmission line and electromagnetic field sensors for DC partial discharge analysis. IEEE Transactions on Dielectrics and Electrical Insulation, 27(6), 2138-2146.

Shibuya, Y., Matsumoto, S., Tanaka, M., Muto, H., & Kaneda, Y. (2010). Electromagnetic waves from partial discharges and their detection using patch antenna. IEEE Transactions on Dielectrics and Electrical Insulation, 17(3), 862-871.

SikorSki, W., Szymczak, C., Siodła, K., & Polak, F. (2018). Hilbert curve fractal antenna for detection and on-line monitoring of partial discharges in power transformers. Eksploatacja i Niezawodność, 20(3), 343-351.

Uwiringiyimana, J. P., Khayam, U., & Montanari, G. C. (2022). Design and implementation of ultra-wide band antenna for partial discharge detection in high voltage power equipment. IEEE Access, 10, 10983-10994.

Vogelsang, R., Sekula, O., Nyffenegger, H., & Weissenberg, W. (2009). Long-term experiences with XLPE cable systems up to 550 kV. Konferenka Siovenskih Electroenergetikov–Kranjska Gora.

Xavier, G. V., da Costa, E. G., Serres, A. J., Nobrega, L. A., Oliveira, A. C., & Sousa, H. F. (2019). Design and application of a circular printed monopole antenna in partial discharge detection. IEEE Sensors Journal, 19(10), 3718-3725.

Yaacob, M., Alsaedi, M. A., Rashed, J., Dakhil, A., & Atyah, S. (2014). Review on partial discharge detection techniques related to high voltage power equipment using different sensors. Photonic sensors, 4(4), 325-337.

Yadam, Y. R., Sarathi, R., & Arunachalam, K. (2022). Planar ultrawideband circularly polarized cosine slot Archimedean spiral antenna for partial discharge detection. IEEE Access, 10, 35701-35711.

Yıldırım, M., & Gözel, M. A. (2023). Asimetrik eş-düzlemsel şerit beslemeli anten ile motor yağ seviye ve kullanim ömrü tespiti. Mühendislik Bilimleri ve Tasarım Dergisi, 11(3), 904-915.

Yıldırım, M., & Gözel, M. A. (2025). High-sensitivity microwave sensor for buffalo milk fat rate and adulteration analysis with branch line coupler. Engineering Science and Technology, an International Journal, 71, 102172.

Zarifi, M. H., Deif, S., Abdolrazzaghi, M., Chen, B., Ramsawak, D., Amyotte, M., Vahabisani, N., Hashisho, Z., Chen, W., & Daneshmand, M. (2017). A microwave ring resonator sensor for early detection of breaches in pipeline coatings. IEEE Transactions on industrial electronics, 65(2), 1626-1635.

Zhang, J., Zhang, X., & Xiao, S. (2017). Antipodal Vivaldi antenna to detect uhf signals that leaked out of the joint of a transformer. International Journal of Antennas and Propagation, 2017(1), 9627649.

Zhang, Z., Assala, P. D. S., & Wu, L. (2018). Residual life assessment of 110 kV XLPE cable. Electric Power Systems Research, 163, 572-580.